Triboelectric-Potential-Regulated Charge Transport Through p–n Junctions for Area-Scalable Conversion of Mechanical Energy

Xian Song Meng, Zhong Lin Wang, and Guang Zhu**

Harvesting ambient mechanical energy is a promising approach to sustainable and maintenance-free power source for electronics that are wireless, stand-alone, and autonomous.[1–8] The sources of mechanical energy cover a wide spectrum of amplitude and frequency. Typical mechanical motions that are usually utilized include vibrations, body movement, and motions in nature such as wind and water waves. Conventional methods of converting mechanical energy mainly rely on piezoelectric effect, electromagnetic effect, and electrostatic induction.[9–17] Recently developed triboelectric generators (TEGs) have shown prominent advantages in power density due to the use of thin-film polymeric materials.[18–20] However, they require either two separate electrodes or a grounded electrode so that net induced charge can be created by charge redistribution.[21,22] Furthermore, they lack a general structure that works for multiple types of mechanical motions.[22–24] More importantly, all the aforementioned energy-harvesting techniques, including the TEG, generate ac output;[25–27] thus phase mismatch among separate devices brings a major problem for constructive and area-scalable integration of a number of devices.

Herein we report the regulation of charge transport direction by the coupling of three effects among triboelectrification, electrostatic induction, and semiconducting properties for converting mechanical energy in an area-scalable way. The change of electric potential induced by a moving triboelectric-charged object alters the Fermi level of a working electrode. For two series-connected p–n junctions that are bridged by the working electrode in between, such an alternation of the Fermi level essentially introduces transient bias voltages of opposite polarities across the two p–n junctions, making one forward biased while the other reverse biased. The asymmetric rectifying property of the junctions makes them act as unidirectional "gates" that regulate the direction of charge transport. As a result, the induced electrons can only flow in a single direction. Theoretical analysis of the electricity-generating process is conducted by analytical calculation and numerical simulation. Based on the above principle, a new class of integrated direct-current triboelectric generators (dc-TEGs) is developed. They can effectively harvest energy from air flow, rotation, and feet motions. The generated electricity can be either stored in batteries or used for applications such as lighting and wireless sensing. Compared to other energy-harvesting techniques including the previously reported TEGs, the integrated dc-TEG possesses several significant advantages. First, it has a planar structure with only one layer of electrode that has extremely small thickness. Second, electricity can be generated regardless of how the external object interacts with the integrated dc-TEG, i.e., either intermittent contacts or continuous sliding. Most importantly, the output current from different units can always constructively add up even though they are not synchronized, which proposes a practical route to scaling up TEGs and other energy-harvesting techniques.

The basic structure of an integrated dc-TEG is illustrated in **Figure 1**. It consists of a "working electrode," two rectifying diodes, an electrification layer, an anode, and a cathode. They are all constructed on top of a flexible substrate. The two diodes made of silicon-based p–n junctions are series connected by the working electrode in between, as shown in Figure 1b. The cathode and the anode are in connection with the p-type and n-type sides of the diodes, respectively. Multiple units share a joint cathode and a joint anode, as shown in Figure 1a,b. The top electrification layer has all components covered beneath. It is made of polytetrafluoroethylene (PTFE) that can be negatively charged by contacting with other materials. The top surface of the electrification layer is modified to create vertical-arrayed PTFE nanorods (Figure 1c) for enhancing the density of triboelectric charge. An as-fabricated integrated dc-TEG that comprises two units is displayed in Figure 1d. The detailed fabrication process is presented in the Experimental Section.

The electricity-generating process of a single unit is illustrated by a cross-sectional view shown in **Figure 2**a. When an external object is in contact with the electrification layer, triboelectric charge of opposite signs is produced at the contact surfaces.[28–31] At this state, net static electric field does not exist, since the positive triboelectric charge is completely screened by its negative counterpart and vice versa.[32] As a result, the Fermi level shown in the band diagram in Figure 2b is horizontally aligned, indicating no charge flow across the entire structure. It is to be noted that the manufactured p–n junctions are heavily doped on the surface to purposely form Ohmic contacts at the metal–semiconductor interface (Figure 2b).

As the contact object leaves away from the electrification layer either vertically or laterally (Figure 2c), the Fermi level of the working electrode, $E_{F(W)}$, is raised because net negative

X. S. Meng, Prof. Z. L. Wang, Prof. G. Zhu
Beijing Institute of Nanoenergy and Nanosystems
Chinese Academy of Sciences
Beijing 100083, China
E-mail: zlwang@binn.cas.cn; zhuguang@binn.cas.cn
Prof. Z. L. Wang
School of Materials Science and Engineering
Georgia Institute of Technology
Atlanta, GA 30332, USA

DOI: 10.1002/adma.201504141

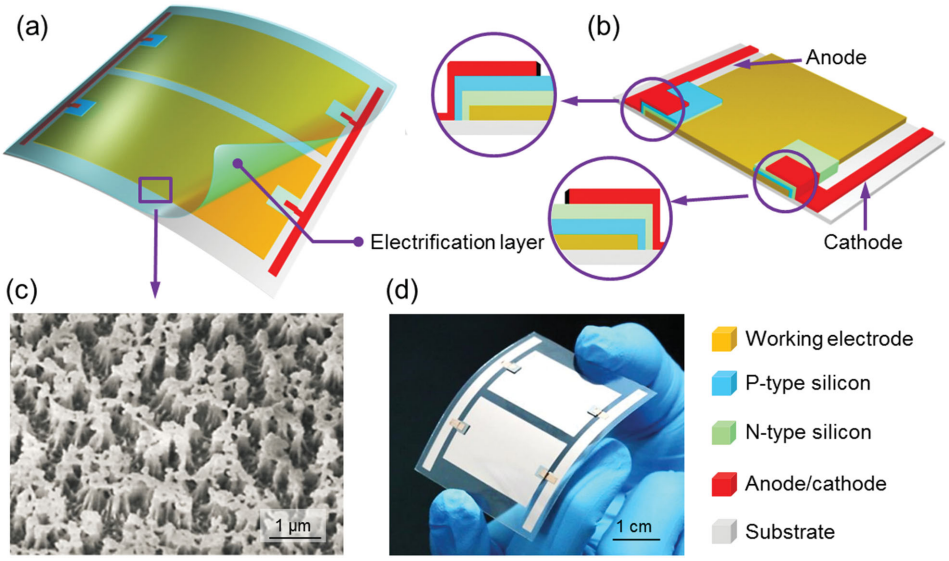

Figure 1. Structure of an integrated dc-TEG: a) schematic of an integrated dc-TEG that has two units; b) schematic of a cross-sectional view that shows the structure of the rectifying diodes; c) SEM image of vertical PTFE nanorods on top of the electrification layer; and d) photograph of an as-fabricated integrated dc-TEG that has two units.

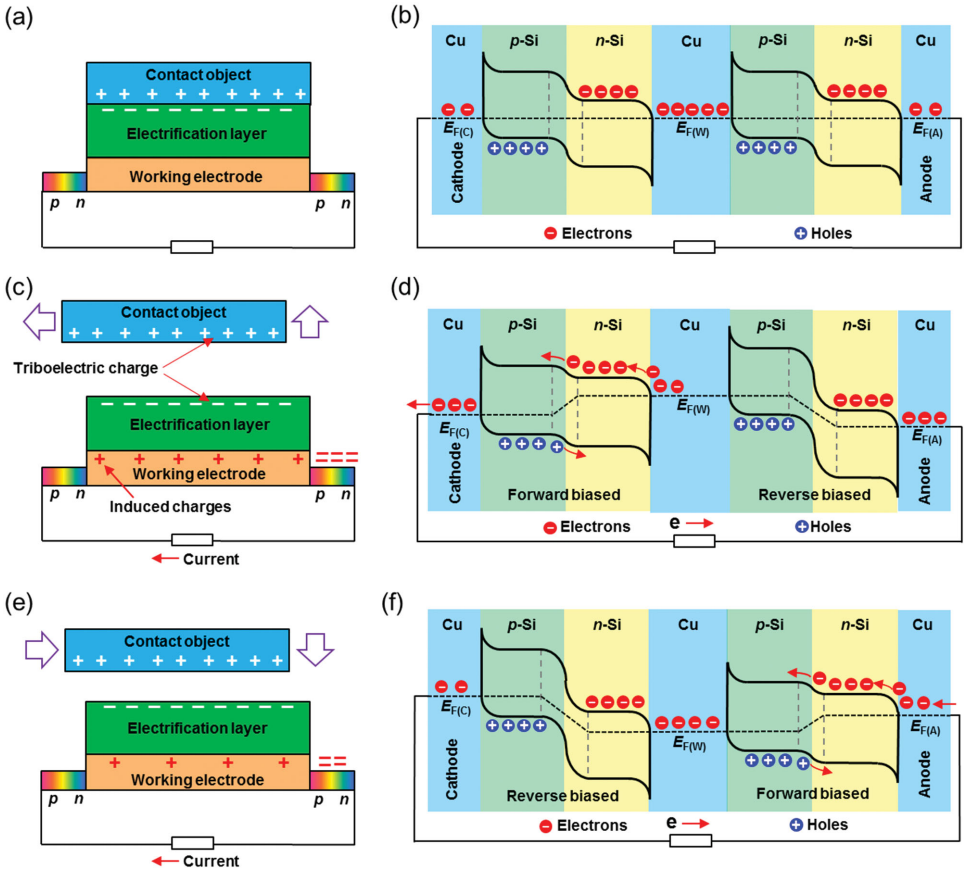

Figure 2. Electricity-generating process: a) simplified diagram in cross-sectional view when the contact object is in close touch with the electrification layer; b) corresponding band diagram in which all Fermi levels are aligned; c) simplified diagram in cross-sectional view when the contact object is separating away from the electrification layer; d) corresponding band diagram in which the left and the right p–n junctions are forward and reverse biased, respectively; e) simplified diagram in cross-sectional view when the contact object is approaching the electrification layer; and f) corresponding band diagram in which the polarity of the bias voltages is reversed.

triboelectric charge introduces a negative electric potential. Then, the $E_{F(W)}$ becomes higher than the Fermi levels of the anode and the cathode, which are denoted as $E_{F(A)}$ and $E_{F(C)}$, respectively. Equivalently, a bias voltage is thus applied across both of the p–n junctions, making the left-hand one in Figure 2d forward biased while the right-hand one reverse-biased since they are series connected. As depicted in Figure 2d, the band diagram is then altered. Driven by the forward bias voltage, free electrons flow from the working electrode to the cathode through the left-hand p–n junction. Subsequently, the extra electrons on the cathode raise the $E_{F(C)}$, driving electrons toward the anode through the external circuit. On the anode side, the reverse-biased p–n junction prevents the electrons from transporting through the junction, leaving the working electrode depleted of electrons and thus positively charged (Figure 2c). As a consequence, induced current is generated, as illustrated in Figure 2c,d. It is to be noted that the change of the band structure is a dynamic process. Therefore, the diagram drawn in Figure 2d only represents a transitional state. As the contact object approaches the electrification layer (Figure 2e), the influence of the negative triboelectric charge diminishes, which lowers the $E_{F(W)}$. Then, the polarities of the bias voltages applied across the two p–n junctions are reversed, making the left-hand one reverse biased while the right-hand one forward biased, as shown in Figure 2f. Based on the similar reasoning above, excessive electrons on the anode side can be propelled back to the working electrode through the forward-biased junction on the right, which replenishes free electrons on the working electrode. Meanwhile, the loss of electrons lowers the $E_{F(A)}$, which again induces electron flow from the cathode to the anode (Figure 2f). From the above analysis, the electricity-generating process is essentially unidirectional flow of electrons from a working electrode as gated by a pair of series-connected rectifying diodes.

To quantitatively interpret the electricity-generating process, we construct a theoretical model that relies on analytical calculation as well as numerical simulation. First, we discuss the case in which the contact object separates away from the electrification layer in the vertical direction (**Figure 3**a). We denote the state shown in Figure 2a as the original state where the electric potential of all components is considered to be zero. In the open-circuit condition, the electric potential of the working electrode $U(t)$ changes linearly with the separation distance, as shown in Figure 3b by COMSOL simulation. If an external load is added, the $U(t)$ can be then expressed by the following equation:

$$U(t) = \frac{\sigma v t}{2\varepsilon_0} + \frac{1}{2\varepsilon_0 S} \times \int_0^t I(t)\,\mathrm{d}t \times \left[vt + \frac{d}{\varepsilon_r} \right] \tag{1}$$

where σ is the triboelectric charge density, v is the uniform velocity of the contact object, t is the time, S is the contact area, $I(t)$ is the output current, d is the thickness of the electrification layer, ε_r is the relative dielectric constant of the electrification layer, and ε_0 is the dielectric constant of vacuum.

The output current $I(t)$ can be obtained by the following equation. Due to low injection condition, the ideal Shockley equation still holds:

$$\begin{aligned} I(t) &= I_{\text{Forward}} - I_{\text{Reverse}} \\ &= I_s \left\{ \text{Exp}\left[\frac{q(U(t) + I(t) \times R/2)}{kT} \right] \right. \\ &\left. - \text{Exp}\left[\frac{-q(U(t) + I(t) \times R/2)}{kT} \right] \right\} \end{aligned} \tag{2}$$

where I_{Forward} and I_{Reverse} are the current through the forward- and reverse-biased p–n junctions, respectively, I_s is the saturation current, q is the electron charge, k is the Boltzmann constant, and T is the temperature in Kelvin.

The detailed derivation of the above equations is discussed in Note S1 (Supporting Information). By substituting constant parameters tabulated in Table S1 (Supporting Information) into Equations (1) and (2), we can get the relationship between the output current and time (Figure 3c). As the load resistance increases, the output current becomes increasingly lower in amplitude and wider in duration. Correspondingly, the output voltage can be obtained simply by multiplying the output current by the load resistance, as displayed in Figure 3d. The average current I_{average} (defined as $\frac{\int_{t_1}^{t_2} I(t)\,\mathrm{d}t}{t_2 - t_1}$, where t_1 and t_2 are times when a current peak starts and ends, respectively) also drops with resistance, while the average voltage ($V_{\text{average}} = I_{\text{average}} \times R$) shows the opposite trend (Figure 3e). As a consequence, the average output power ($V_{\text{average}} \times I_{\text{average}}$) reaches the maximum value of 14 mW at a uniform moving velocity of 0.3 m s^{-1} (Figure 3f). Similarly, for the case in which the contact object slides laterally as shown in Figure 3g, the electric potential of the working electrode in the open-circuit condition also rises as the object slides apart (Figure 3h). The numerically calculated output current and voltage at different load resistance are exhibited in Figure 3i,j, respectively. At a sliding velocity of 1 m s^{-1}, the average current is calculated to be 7 μA in the short-circuit condition and drops with resistance (Figure 3k). Correspondingly, the maximum average power of 55 mW can be obtained (Figure 3l).

To verify the proposed theoretical model, an electricity-generating unit is fabricated for electrical measurement. Its working electrode has lateral dimensions of 50 mm by 30 mm. A moving object made of latex exerts vertical impacts onto the electrification layer in a reciprocating way (**Figure 4**a). The produced short-circuit current (I_{sc}) exhibits sharp peaks in a single direction in Figure 4b, which has average amplitude of 220 μA. The magnified view in Figure 4c reveals that a complete motion cycle actually generates two peaks. A higher one corresponding to the approaching process is immediately followed by a smaller and wider one that comes from the separating process (Figure 4c). The difference in amplitude is due to asymmetric velocities of the reciprocating motion. In contrast, if the p–n junctions are placed back-to-back or head-to-head, the output current becomes negligible, which is shown in Figure S1 (Supporting Information). As the object leaves away, the quantity of induced charge flowing through the external circuit keeps increasing until saturation takes place when the object moves beyond 22 mm (Figure 4d). Further motion no longer causes variation of the electric potential on the working electrode, which is the reason for the saturation. Though it is clearly observed that the motion velocity of the object can considerably alter the

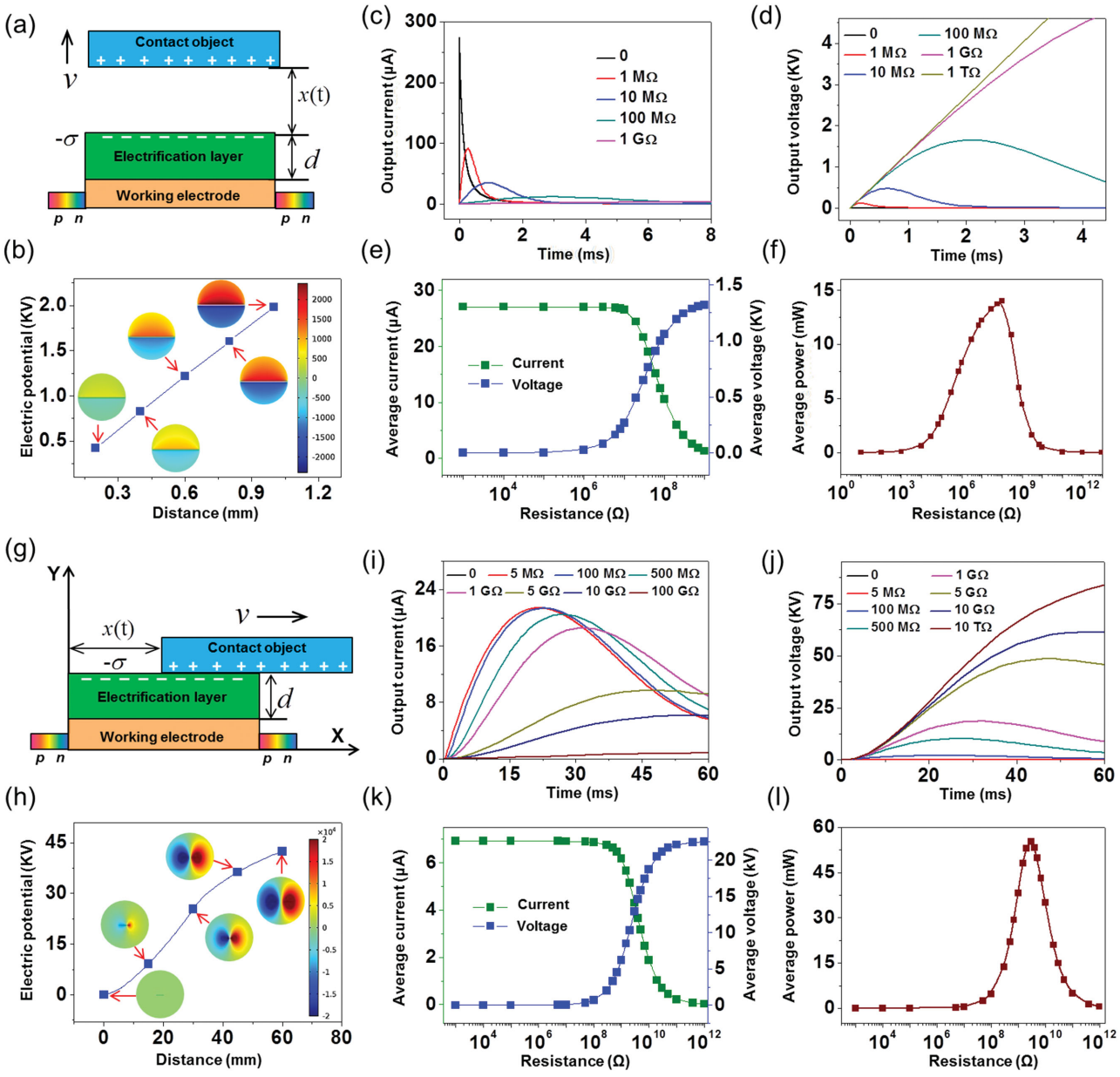

Figure 3. Theoretical results of the electric output: a) simplified diagram in cross-sectional view when the contact object moves vertically; b) simulated electric potential via COMSOL on the working electrode as the object separates away in open-circuit condition; c) theoretical output current curves at different loads (velocity: 0.3 m s^{-1}); d) theoretical output voltage curves at different loads (velocity: 0.3 m s^{-1}); e) theoretical values of the average current and voltage as influenced by load resistance (velocity: 0.3 m s^{-1}); f) theoretical values of the average power as influenced by load resistance (velocity: 0.3 m s^{-1}); g) simplified diagram in cross-sectional view when the contact object slides laterally; h) simulated electric potential via COMSOL on the working electrode as the object slides apart in open-circuit condition; i) theoretical output current curves at different loads (sliding velocity: 1 m s^{-1}); j) theoretical output voltage curves at different loads (sliding velocity: 1 m s^{-1}); k) theoretical values of the average current and voltage as influenced by load resistance (sliding velocity: 1 m s^{-1}); and l) theoretical values of the average power as influenced by load resistance (sliding velocity: 1 m s^{-1}).

current amplitude, it does not affect the quantity of induced charge that depends on the object position instead (Figure 4e). At a velocity of 0.5 m s^{-1}, the average current $I_{average}$ decreases if external load resistance increases over 10^5 Ω. Correspondingly, the average power calculated by $I_{average} \times R^2$ reaches the maximum value of 14.8 mW at the optimal resistance of 10^8 Ω (Figure 4f). It is noticed that the optimum load is very high, which may cause load (or matching) problems. This issues can be mitigated by using power management circuits.[2] The average power is approximately linearly related to the velocity. We noticed that the optimal load resistance gradually shifts to left, as revealed in Figure 4g. This is because higher current corresponds to lower output impedance of the dc-TEG, making the impedance matching point shift to lower value.

Electrical measurement was also conducted when the object laterally slides against the electrification layer (Figure 4h). The

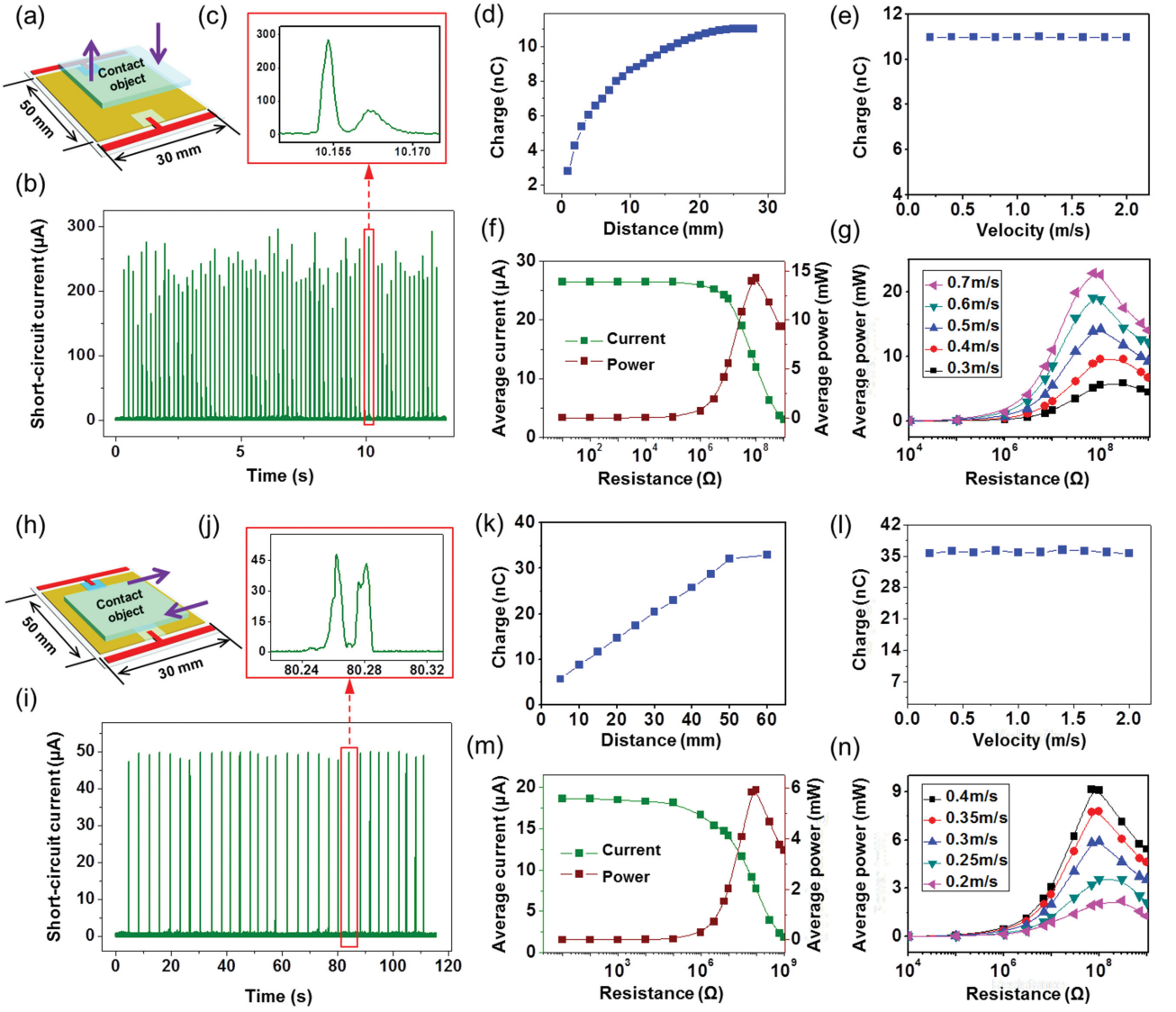

Figure 4. Experimental results of the electric output: a) simplified diagram when the contact object has reciprocating motion in vertical direction; b) short-circuit current (velocity: 5 m s^{-1}); c) zoom-in view of the short-circuit current in a single cycle of the movement; d) quantity of induced charge that transports between electrodes as the object separates away; e) relation between the quantity of induced charge and the moving velocity (separation distance: 25 mm); f) average current and average power as influenced by load resistance (velocity: 0.5 m s^{-1}); g) average power as influenced by load resistance at different velocities; h) simplified diagram when the contact object has reciprocating motion in lateral direction; i) short-circuit current (velocity: 1 m s^{-1}); j) zoom-in view of the short-circuit current in a single cycle of the movement; k) quantity of induced charge that transports between electrodes as the object slides apart; l) relation between the quantity of induced charge and the moving velocity (sliding distance: 55 mm); m) average current and power as influenced by load resistance (velocity: 0.3 m s^{-1}); and n) average power as influenced by load resistance at different velocities.

I_{sc} has peaks in only one direction as expected (Figure 4i). A cycle of reciprocating motion also produces two current peaks, which is revealed by the zoom-in view in Figure 4j. The two peaks have comparable amplitudes because of symmetric motion velocities. As the contact object partially slides apart, the quantity of induced charge flowing through the external circuit is linearly related to the sliding distance until the object gets completely apart (Figure 4k). Similar to the case where the object has vertical contacts in Figure 4a, the total induced charge generated in a single motion cycle is independent on the sliding velocity (Figure 4l). At a sliding velocity of 0.3 m s^{-1}, the maximum average power reaches 6 mW (Figure 4m). As shown in Figure 4n, the average power curves also shift to the left as the sliding velocity increases.

Based on the above theoretical analysis and the obtained experimental data, the novel principle enables a dc output no matter how an external object interacts with the device. This unique feature brings about significant benefits in practical use of the TEG. A number of units can be effectively integrated because the output current from individual ones can always constructively add up, even though their current output may not be synchronized. To further demonstrate this advantage, we designed and fabricated three types of integrated dc-TEGs for specific purposes.

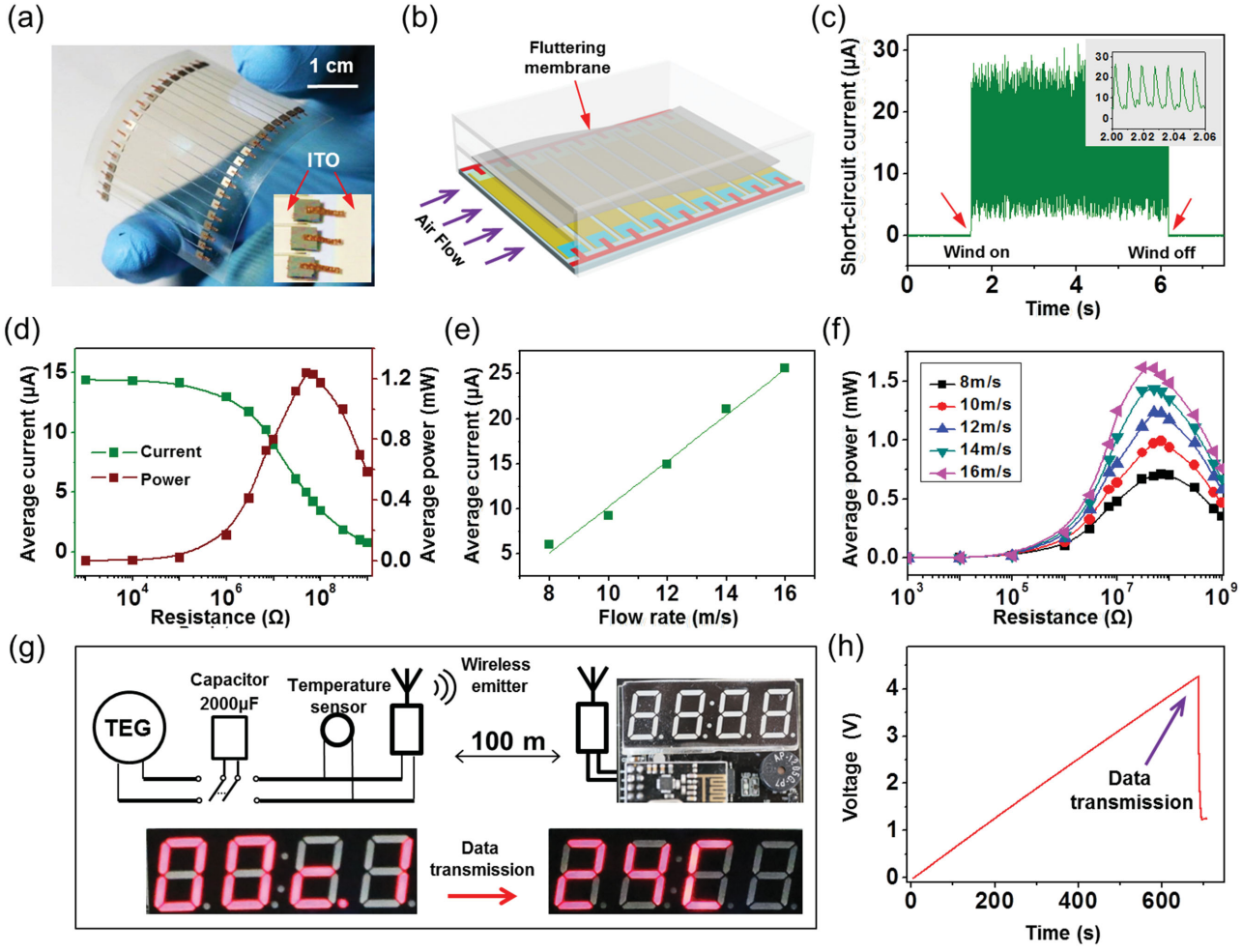

Figure 5. Harvesting wind energy by an integrated dc-TEG: a) photograph of the as-fabricated integrated dc-TEG (inset: ITO as electrodes); b) structural schematic of the device for harvesting wind energy; c) short-circuit current at a flow rate of 10 m s^{-1} (inset: zoom-in view); d) average current and average power as influenced by load resistance at a flow rate of 10 m s^{-1}; e) average current in short-circuit condition short-circuit as a function of the flow rate; f) average power as influenced by load resistance at different flow rates; g) self-powered temperature sensing and wireless data transmission; and h) voltage of a capacitor (2000 μF) as it is being charged and discharged.

First, it was applied in harvesting wind energy. An integrated dc-TEG having a total of 15 units in an array was fabricated on a transparent flexible polyethylene terephthalate substrate. It has lateral dimensions of 50 mm by 30 mm. All of the units share a joint cathode and joint anode. ITO was used as a conductive material of the working electrode, making the integrated dc-TEG transparent, as displayed in **Figure 5**a. Driven by air flow, a freestanding polymer membrane flutters and periodically contacts with the electrification layer underneath,[5,33] as sketched in Figure 5b. As a result, electricity is produced, which is shown by the current pack in Figure 5c. At an air flow rate of 10 m s^{-1}, the current amplitude exceeds 30 μA; and the average current is calculated to be 14.8 μA. It is observed in the magnified inset (Figure 5c) that the current pack consists of periodic peaks. Each current peak results from a unit because the fluttering membrane interacts with the arrayed-units sequentially instead of simultaneously. Load matching curves in Figure 5d show the maximum average power as high as 1.2 mW. It presents at least 30-fold enhancement over previous reports in which a conventional structure without the array was used.[34] The air flow directly governs the electric output since it is a measure of the input mechanical energy. As the flow rate increases, the average current in short-circuit condition is linearly enhanced (Figure 5e) and so is the average power. It is noticed that a decent output power of 0.7 mW can be generated at a flow rate of 8 m s^{-1} (Figure 5f). This flow rate corresponds to moderate breeze at level 4 according to the Beaufort scale, which proves the usability of the integrated dc-TEG in a mild condition. The integrated dc-TEG was then demonstrated as the sole power source for a wireless sensing system that is diagramed in Figure 5g. It took 650 s for the integrated dc-TEG to charge a 2000 μF capacitor to 4.3 V (Figure 5h). The stored energy could then power the temperature sensor and transmit a pack of wireless data so that the temperature information could be displayed at the receiving end that could be as far as 100 m away (Figure 5g; Movie S1, Supporting Information). Therefore, self-powered wireless sensing for such uses as environmental monitoring is demonstrated to be feasible.

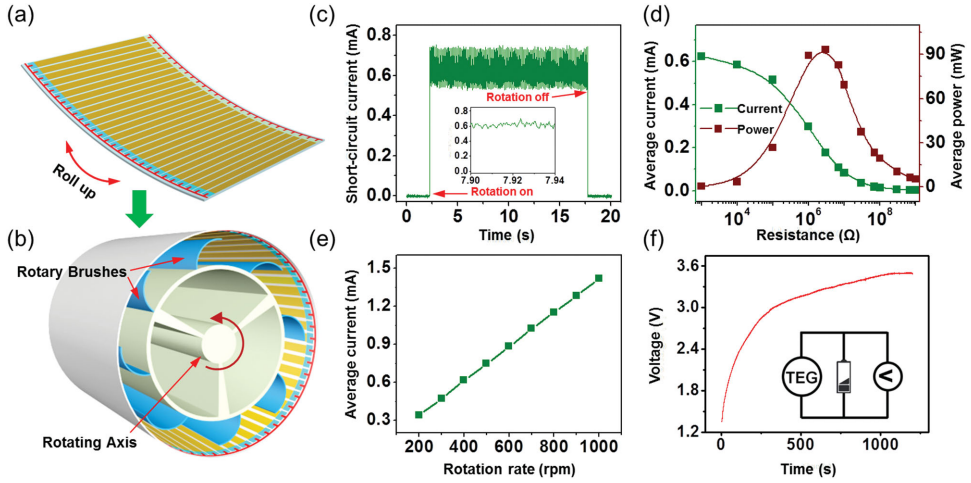

Figure 6. Harvesting energy from rotation by an integrated dc-TEG: a) schematic of the integrated dc-TEG that can be rolled up; b) schematic of the entire setup in which an array of flexible rotary brushes is used; c) short-circuit current at a rotation rate of 500 rpm (inset: zoom-in view); d) average current and average power as influenced by load resistance at a rotation rate of 500 rpm; e) average current in short-circuit condition short-circuit as a function of the rotation rate; and f) voltage of a battery (7 mAh) as it is being charged at a rotation rate of 500 rpm.

Second, this novel structure was used to harness rotation. Having 80 units in total and lateral dimensions of 80 mm by 70 mm, an integrated dc-TEG was rolled up to form a cylinder (**Figure 6**a). An array of 30 brushes made of flexible polyamide sheets are fastened on a rotating axis in the center (Figure 6b). As the axis spins, the bent brushes continuously slide on the electrification layer. The I_{sc} has an average value of 0.62 mA at a rotation rate of 500 rpm, which is exhibited in Figure 6c. Correspondingly, the maximum average power shoots to over 93 mW at the optimal load resistance of 3 MΩ (Figure 6d). Despite of minor fluctuation as shown in the inset (Figure 6c), the current remains successive instead of being intermittent. This is caused by the fact that numerous current peaks from individual units constructively add together. Higher rotation rate can linearly promote the output current (Figure 6e). For a lithium ion battery having a capacity of 7 mAh, it can be charged by the produced electricity from 1.3 to 3.5 V in 18 min when the integrated dc-TEG rotates at 500 rpm (Figure 6f). The demonstration reveals that constructive addition of the electricity from individual units can be realized.

Moreover, the units can be integrated into a 2D array over a large area to become a "power carpet." As shown by the picture in **Figure 7**a, a 36-unit array is integrated on a flexible textile substrate. Each unit has a side length of 5 cm. The connection method is schemed in Figure 7b. Alternating cathodes and anodes are placed in lines, which are labeled in Figure 7a. Conductive fabric-based textile was used as the material for the working electrode to make the entire device flexible, bendable, and rollable, as shown in Figure 7c. The PTFE fabric was adopted as the electrification material, making the device entirely fabric-based. An as-fabricated device is exhibited in Figure 7d. If spread on the floor, it can scavenge energy from interactions with shoes. As clearly demonstrated in Figure 7e, output current can be produced by diverse types of motions including walking, running, jumping, and sliding friction. As explained above, the current amplitude is related to how fast the interaction is. Thus, jumping corresponds to the highest and sharpest current peaks among all types of motions, as shown in the magnified insets of Figure 7e. The produced electricity can directly power a number of small electronics (Figure 7f; Movie S2, Supporting Information). If this area-scalable "power carpet" (Figure 7g) can be used in places that have large flows of people such as subway stations and shopping malls, the produced electric energy in total may become considerable.

In summary, we report a new class of integrated dc-TEG based on the novel coupling of three-effects among triboelectrification, electrostatic induction, and semiconducting properties. The asymmetric rectifying property of the p–n junctions makes them act as unidirectional "gates" that regulate the induced charge to transport in a single direction. Metal–semiconductor Schottky contacts that are also rectifying may replace the p–n junction, which can further simplify the structure. Compared to previously reported TEGs, the integrated dc-TEG has a planar structure with only one layer of electrode that has an extremely small thickness. Besides, electricity can be generated regardless of how a charged external object interacts with the integrated dc-TEG. Most importantly, output current from different units can always constructively add up, thus presenting a feasible route to large-area applications of the TEG and other energy-harvesting techniques.

Experimental Section

Fabrication of an Integrated dc-TEG: (1) A PET substrate (50 μm in thickness) of desired dimensions was prepared by laser cutting. (2) A PET-based mask with hollow windows that define the positions and dimensions of the working electrodes, the anode, and the cathode was also prepared by laser cutting. (3) Via sputtering (dc-sputtering for metal and rf-sputtering for ITO), the predefined electrodes (200 nm in thickness) were deposited onto the PET substrate. (4) The bottom side the p–n junctions were adhered onto the working electrodes by silver epoxy; the top side of junctions was connected to either anode or cathode by adhesive copper tapes. (5) A PTFE film of 25 μm in thickness (adhesive on one side) was mounted onto the electrodes. (6) PTFE nanorods were created by ICP etching. Before etching, a layer of Au of

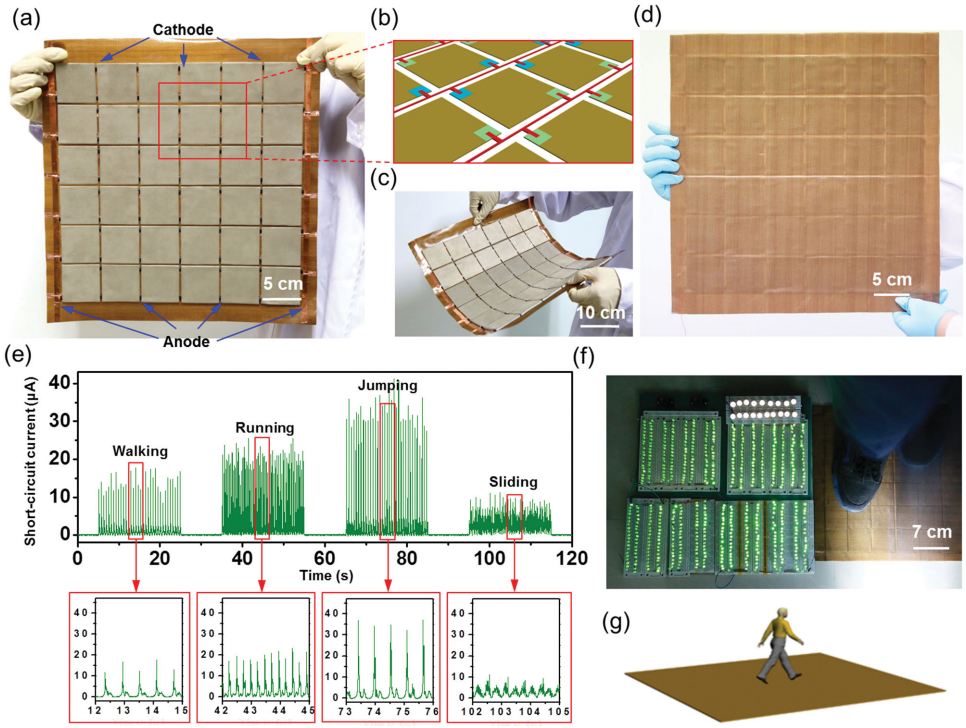

Figure 7. Energy harvesting by a "power carpet": a) photograph of a textile-based integrated dc-TEG fabricated on a flexible substrate; b) schematic of connection configuration of the unit array; c) photograph of the bent integrated dc-TEG; d) photograph of a completed as-fabricated "power carpet"; e) short-circuit current resulting from different types of interactions between the carpet and shoes (insets: zoom-in views of the current); f) photograph of hundreds of illuminated LEDs powered by the carpet when being walked over; and g) schematic that visions area-scalable implementation.

10 nm in thickness was sputtered onto the PTFE surface as catalyst. Ar, O_2, and CF_4 gases were fed into the ICP chamber with flow rates of 15.0, 10.0, and 30.0 sccm (standard cubic centimeter per minute), respectively. The operation temperature was 55.0 °C with a pressure of 15 mTorr. One power source of 400 W was used to generate a large density of plasma while another power source of 100 W was used to accelerate plasma ions toward the polymer surface.

Fabrication of the "Power Carpet": Electrodes of the "power carpet" were made of conductive copper-coated textile that can be commercially obtained. PTFE textile was used as the electrification layer with one-side adhesive, which can also be purchased. The working electrodes, cathode, and anode were all prepared by laser cutting to obtain desired dimensions. Chips of the p–n junctions were placed at the diagonal positions of the working electrodes that are square-shaped.

Supporting Information

Supporting Information is available from the Wiley Online Library or from the author.

Acknowledgements

X.S.M. and G.Z. contributed equally to this work. The research was supported by the Chinese "Thousands Talents" program for pioneer researchers. Patents have been filed based on the research presented here.

Received: August 24, 2015
Revised: September 27, 2015
Published online: November 27, 2015

[1] Z. L. Wang, J. Song, *Science* **2006**, *312*, 242.
[2] G. Zhu, J. Chen, T. Zhang, Q. Jing, Z. L. Wang, *Nat. Commun.* **2014**, *5*, 3426.
[3] T. Thundat, *Nat. Nanotechnol.* **2008**, *3*, 133.
[4] A. Varpula, S. J. Laakso, T. Havia, J. Kyynäräinen, M. Prunnila, *Sci. Rep.* **2014**, *4*, 6799.
[5] J. Bae, J. Lee, S. Kim, J. Ha, B.-S. Lee, Y. Park, C. Choong, J.-B. Kim, Z. L. Wang, H.-Y. Kim, *Nat. Commun.* **2014**, *5*, 4929.
[6] B. Y. Lee, J. Zhang, C. Zueger, W.-J. Chung, S. Y. Yoo, E. Wang, J. Meyer, R. Ramesh, S.-W. Lee, *Nat. Nanotechnol.* **2012**, *7*, 351.
[7] R. Vullers, R. van Schaijk, I. Doms, C. Van Hoof, R. Mertens, *Solid-State Electron.* **2009**, *53*, 684.
[8] J. Briscoe, M. Stewart, M. Vopson, M. Cain, P. M. Weaver, S. Dunn, *Adv. Energy Mater.* **2012**, *2*, 1261.
[9] N. Jalali, P. Woolliams, M. Stewart, P. M. Weaver, M. G. Cain, S. Dunn, J. Briscoe, *J. Mater. Chem. A* **2014**, *2*, 10945.
[10] X. Chen, S. Xu, N. Yao, Y. Shi, *Nano Lett.* **2010**, *10*, 2133.
[11] N. W. Hagood, A. von Flotow, *J. Sound Vib.* **1991**, *146*, 243.
[12] X. Wang, *Nano Energy* **2012**, *1*, 13.
[13] S. P. Beeby, R. Torah, M. Tudor, P. Glynne-Jones, T. O'Donnell, C. Saha, S. Roy, *J. Micromech. Microeng.* **2007**, *17*, 1257.
[14] O. Zorlu, E. T. Topal, H. Kulah, *IEEE Sens. J.* **2011**, *11*, 481.
[15] P. Basset, D. Galayko, A. M. Paracha, F. Marty, A. Dudka, T. Bourouina, *J. Micromech. Microeng.* **2009**, *19*, 115025.
[16] C. Williams, R. B. Yates, *Sens. Actuators, A* **1996**, *52*, 8.
[17] A. Khaligh, P. Zeng, C. Zheng, *IEEE Trans. Ind. Electron.* **2010**, *57*, 850.
[18] F.-R. Fan, Z.-Q. Tian, Z. L. Wang, *Nano Energy* **2012**, *1*, 328.
[19] S.-H. Shin, Y. H. Kwon, Y.-H. Kim, J.-Y. Jung, M. H. Lee, J. Nah, *ACS Nano* **2015**, *9*, 4621.

[20] K. Y. Lee, J. Chun, J. H. Lee, K. N. Kim, N. R. Kang, J. Y. Kim, M. H. Kim, K. S. Shin, M. K. Gupta, J. M. Baik, *Adv. Mater.* **2014**, *26*, 5037.
[21] Y. Yang, H. Zhang, J. Chen, Q. Jing, Y. S. Zhou, X. Wen, Z. L. Wang, *ACS Nano* **2013**, *7*, 7342.
[22] G. Zhu, C. Pan, W. Guo, C.-Y. Chen, Y. Zhou, R. Yu, Z. L. Wang, *Nano Lett.* **2012**, *12*, 4960.
[23] H. Guo, Q. Leng, X. He, M. Wang, J. Chen, C. Hu, Y. Xi, *Adv. Energy Mater.* **2015**, *5*, 1400790.
[24] X. Cheng, B. Meng, X. Zhang, M. Han, Z. Su, H. Zhang, *Nano Energy* **2015**, *12*, 19.
[25] M. Ha, J. Park, Y. Lee, H. Ko, *ACS Nano* **2015**, *9*, 3421.
[26] Z. L. Wang, *ACS Nano* **2013**, *7*, 9533.
[27] J. Briscoe, N. Jalali, P. Woolliams, M. Stewart, P. M. Weaver, M. Cain, S. Dunn, *Energy Environ. Sci.* **2013**, *6*, 3035.
[28] R. G. Horn, D. T. Smith, *Science* **1992**, *256*, 362.
[29] R. G. Horn, D. T. Smith, A. Grabbe, *Nature* **1993**, *366*, 442.
[30] M. M. Apodaca, P. J. Wesson, K. J. Bishop, M. A. Ratner, B. A. Grzybowski, *Angew. Chem.* **2010**, *122*, 958.
[31] H. Baytekin, A. Patashinski, M. Branicki, B. Baytekin, S. Soh, B. A. Grzybowski, *Science* **2011**, *333*, 308.
[32] S. Niu, S. Wang, L. Lin, Y. Liu, Y. S. Zhou, Y. Hu, Z. L. Wang, *Energy Environ. Sci.* **2013**, *6*, 3576.
[33] Y. Yang, G. Zhu, H. Zhang, J. Chen, X. Zhong, Z.-H. Lin, Y. Su, P. Bai, X. Wen, Z. L. Wang, *ACS Nano* **2013**, *7*, 9461.
[34] X. S. Meng, G. Zhu, Z. L. Wang, *ACS Appl. Mater. Interfaces* **2014**, *6*, 8011.